

## Imaging and suppressing near-receiver scattered surface waves

Xander H. Campman<sup>1</sup>, Kasper van Wijk<sup>2</sup>, John A. Scales<sup>2</sup>, and Gérard C. Herman<sup>1,3</sup>

### ABSTRACT

When traveling through a complex overburden, upcoming seismic body waves can be disturbed by scattering from local heterogeneities. Currently, surface-consistent static and amplitude corrections correct for rapid variations in arrival times and amplitudes of a reflector, but these methods impose strong assumptions on the near-surface model. Observations on synthetic and laboratory experiments of near-surface scattering with densely sampled data suggest that removing noise from near-receiver scattering requires multichannel approaches rather than single-channel, near-surface corrections.

In this paper we develop a wavefield-based imaging method to suppress surface waves scattered directly beneath the receivers. Using an integral-equation formulation, we account for near-surface heterogeneities by a surface impedance function. This impedance function is used to model scattered surface waves, excited by upcoming wavefronts. The final step in our algorithm is to subtract the scattered surface waves. We successfully apply this method to laboratory data of scattered surface waves, excited and monitored with a noncontacting acquisition system.

### INTRODUCTION

Scattered surface waves can be a major source of coherent noise in seismic records. For land data, most of the source energy is converted into surface (Rayleigh) waves (e.g., Aki and Richards, 1980) that can be scattered by surface topography or near-surface heterogeneities and mask reflections from deeper structures (Blonk and Herman, 1994; Regone, 1998). This type of scattering of shot-generated surface waves is usually referred to as side scattering. But surface waves

can also be excited by body-wave reflections impinging on heterogeneities directly beneath the receivers. In this case, body waves are converted into (scattered) surface waves because heterogeneities act like secondary sources. Body waves are also converted to scattered P- and S-waves, but we restrict our discussion to surface waves since they form the most significant part of the scattered wavefield. In global seismology, Wagner and Langston (1992) note that body-to-surface wave scattering explains part of the coda of teleseismic P-wave, while Gupta et al. (1990) use this type of scattered wave to locate near-array scattering sources. Moreover, P-wave to Rayleigh-wave scattering is a cause of noise in receiver-function studies (e.g., Kennett, 2002). In exploration seismology, Combee (1994, 1995) studies scattering by near-receiver and near-source heterogeneities. Because the strength of scattered waves is proportional to the strength of the incident reflection, this type of scattered energy can be considered multiplicative noise.

Multiplicative noise from an isolated scatterer appears as a diffraction, perhaps including resonances. This becomes especially clear in densely sampled data. But as the near-surface becomes more complex, scattering from different heterogeneities interferes and the noise can appear as rapid (trace-to-trace) variations in the arrival times and amplitudes of reflections. For many randomly distributed scatterers, such complex scattering behavior is shown in Riyanti and Herman (2004). Since all upcoming reflections impinge on the same heterogeneities close to the receivers, the scattering degrades the continuity of reflectors throughout the record, which makes this kind of noise fundamentally different from side-scattered, or additive, noise.

To see this, consider the situation sketched in Figure 1, where the source  $S$  excites both body and surface waves. The shot-generated surface wave travels along path  $a$  and scatters far from the source and receivers; it is recorded at geophone  $G$ . In this case, the interaction takes place between surface waves only. The body wave, however, first travels downward, where it is eventually reflected partly into upcoming body

Manuscript received by the Editor October 14, 2003; revised manuscript received February 18, 2004; published online March 22, 2005.

<sup>1</sup>Delft University, Applied Mathematics, Mekelweg 4, 2628 CD, Delft, The Netherlands. E-mail: campman@ewi.tudelft.nl; g.c.herman@ewi.tudelft.nl.

<sup>2</sup>Colorado School of Mines, Physical Acoustics Laboratory, 1500 Illinois St., Golden, Colorado 80401. E-mail: kasper@ruelle.mines.edu; jscales@lepton.mines.edu.

<sup>3</sup>Presently Shell International E & P, P.O. Box 60, 2280 AB, Rijswijk, ZH, The Netherlands.

© 2005 Society of Exploration Geophysicists. All rights reserved.

waves. These upcoming waves travel through the overburden and can be scattered by heterogeneities close to the receivers where they excite surface waves. In this way, all upcoming body-wave reflections are partly converted into surface waves.

Currently, residual static correction techniques correct for trace-to-trace time and amplitude variations. These techniques are based on a model that assigns the same uniform time shift or filter to each trace from a distinct surface location, assuming vertical raypaths through the overburden. For an extensive overview of static correction methods and the underlying principles, refer to Cox (1999). Although based on a simple transmission model of the subsurface, these techniques can be effective in many cases. However, when the subsurface is strongly heterogeneous, this transmission model does not explain the observed scattered energy. Neglecting (multiply) scattered waves can degrade the high-frequency content of the data because of destructive interference of rapidly varying traces during stacking [as quantified in connection with short-wavelength residual statics by Cox (1999, chapter 6)], and it may introduce phase distortions.

Methods based on the apparent velocity of surface waves (e.g., Yilmaz, 1987) effectively suppress the scattered tails — i.e., the part of the scattered surface wave with linear move-out — but cannot remove certain parts of the scattered waves with higher apparent velocities. In this paper, we discuss a method to attenuate all parts of the scattered surface waves that interfere with reflections throughout the record and thereby degrade their continuity.

We estimate a surface-impedance function of the region directly under the receivers using inverse scattering and subsequently predict and subtract the scattered surface waves for the entire record, improving resolution of target reflections. The method is based on an integral-equation formulation of the scattering process near the surface. For the case of source-generated surface waves scattered far from the receivers, Blonk and Herman (1994) show that near-surface scattering can be accounted for by a 2D impedance function, drastically reducing computation costs. In our formulation, we assume this to be valid for near-receiver scattering as well. The method outlined in this paper is a generalization of a similar method for attenuating scattered tube waves in vertical seismic profiling (VSP) records, discussed in Herman et al. (1999).

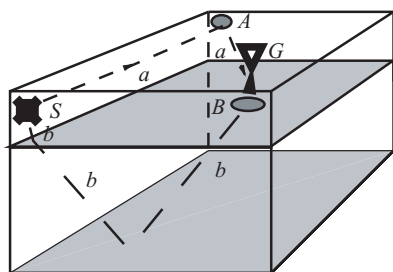


Figure 1. Two types of near-surface scattering mechanisms. *A* is a heterogeneity far from the source *S* and receiver *G*; shot-generated surface waves travel along path *a* and are scattered at *A*. This is a form of side-scattered or additive noise. *B* is a heterogeneity directly beneath the receiver. Body waves travel along path *b* and are reflected by layers. Each reflection recorded by *G* passes through *B* and excites (scatters) surface waves.

We validate our method on scale-model data, where we excite and measure ultrasonic wavefields scattered near the surface of an aluminum block. In these experiments, we measure the vertical velocity on the surface of the aluminum block with a scanning laser interferometer. This noncontacting data acquisition allows for receiver intervals much less than the dominant wavelength, much like the dense receiver arrays developed in exploration seismics (Baeten et al., 2000). With this dense sampling we are able to monitor the complete wavefield without spatial aliasing, greatly contributing to our understanding of the near-surface scattering problem.

## NEAR-SURFACE SCATTERING VERSUS STATICS

For an extensive overview of work done on various aspects of near-surface scattering, refer to Levander (1990). Combee (1994) isolates the problem of an upcoming plane scalar wave incident on a near-surface anomaly and presents analytical solutions. He concludes that for anomaly sizes on the order of a wavelength, multiple scattering changes the wavelet in a way that cannot be accounted for by static corrections. Here, we present a similar study, using a 2D elastic finite-difference code to model the response of the wavefield excited by a plane-wave source at the bottom of a two-layered model. This type of model accounts for conversion of body waves into surface waves and guided waves.

A schematic of the model is shown in Figure 2. The top layer has a P-wave velocity given by  $c_P = 1200$  m/s and an S-wave velocity given by  $c_S = 400$  m/s. In the middle of the model, the depth of the top layer (2 m) changes to 10 m and back. The P-wave velocity in the base layer is  $c_P = 2500$  m/s, while the S-wave velocity in the base layer is  $c_S = 600$  m/s. The vertical component of the particle velocity, calculated at the surface, is shown as a function of time and position in Figure 3a. In this figure, we simulate field arrays by averaging over 10 m. In Figure 3b the original record of single receivers with a spacing of 2 m is shown. This section contains a shift — consistent with a static shift calculated along vertical raypaths — around 25 ms and interference of around 70 ms as a result of multiple scattering. At later times, one can identify guided waves traveling outward from the anomaly. In Figure 3c we align the traces at first breaks. Clearly, this (simple) static correction

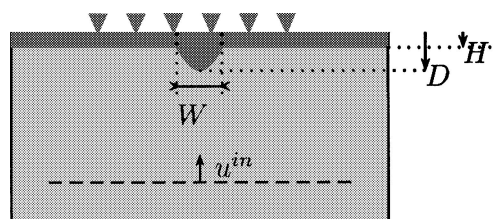


Figure 2. Model with a layer and anomaly. The velocities of the top layer and the anomaly are the same:  $c_P = 1200$  m/s and  $c_S = 400$  m/s. The velocities of the second layer are  $c_P = 2500$  m/s and  $c_S = 600$  m/s, respectively. To simulate an upcoming reflection, a plane-wave source, with dominant frequency of about 20 Hz, is located at 25-m depth. The dimensions are  $W \approx 20$  m,  $D = 10$  m, and  $H = 2$  m. The value  $u^{in}$  is the incident wavefield.

does not restore continuity of the event, and stacking these corrected traces will produce nearly the same array-formed stack as the one shown in Figure 3a. In the array-formed data, the anomaly appears in the form of a static with additional amplitude and phase distortions, while in the original single-receiver data, the anomaly is characterized by scattering, including the shift and interference. Because scattering and related phenomena like interference are deterministic, multi-channel processes, one can infer that the proper way to correct for the anomaly is a multichannel approach before array forming (Blacquière and Ongkiehong, 2000). Discussing intra-array processing, Baeten et al. (2001) raise a similar point. They show that intra-array static corrections can be effective, but they note that perturbations from diffractions and reverberations require wavefield-based inversion methods. In general, part of the guided wave with linear moveout can be removed with velocity filtering techniques, but this will leave the apex of the scattered wavefield unaffected and the interference will remain. Removing this part of the scattered noise requires a wavefield-based method.

## METHOD

### Scattered-noise model

The objective of our method is to obtain an estimate of the wavefield without scattered energy from near-surface heterogeneities. On account of linearity of the elastic wavefield, the vertical velocity component  $v(\mathbf{x}, t)$ , measured at position  $\mathbf{x} = (x, y, z)$  excited by a fixed vertical point source, can be written as

$$v(\mathbf{x}, t) = v^0(\mathbf{x}, t) + v^1(\mathbf{x}, t). \quad (1)$$

Here,  $v$  is the measured field,  $v^0$  is the field that would have been measured if the overburden were homogeneous, and  $v^1$  is the part of the wavefield that accounts for scattering from heterogeneities close to the acquisition surface. Thus, we want an estimate of  $v^0$ . Our approach is to find the scattered noise  $v^1$  and then to subtract it from the data. Here, we consider the case in which we measure only the vertical velocity.

From the elastic-wave equation for particle displacement, we can derive an approximate integral representation for the scattered noise in terms of vertical particle velocity, measured at the surface  $z_0$  (Blonk and Herman, 1994):

$$v^1(\mathbf{x}_l, z_0, \omega) = \int_{\mathbf{x}'_l \in \Sigma} u_z^G(\mathbf{x}_l - \mathbf{x}'_l, \Delta z, \omega) \times \sigma(\mathbf{x}'_l, z_1, \omega) v(\mathbf{x}'_l, z_1, \omega) d\mathbf{x}'_l, \quad (2)$$

where  $u_z^G$  is the vertical component of the Green's displacement tensor attributed to a vertical point force, derived for a homogeneous half-space in Appendix A. Horizontal position is denoted by  $\mathbf{x}_l = (x, y)$ ,  $z_1$  is the scattering depth, and  $\Delta z = z_0 - z_1$ . The impedance function is denoted by  $\sigma$ ;  $\omega$  is angular frequency. The surface  $\Sigma$  is the area occupied by the receivers (i.e., the acquisition surface). If the scattering takes place close to the surface ( $z_1 \approx z_0$ ), we measure the wavefield just above the scatterer and then we can approximate the field at  $z_1$  by the field recorded at depth  $z_0$ . In this way, we can calculate the scattered field  $v^1$  once  $\sigma$  is known. Note that the integral is over a surface; thus, we express scattering by a scattering volume in terms of a surface impedance function.

This type of approximation is also used for surface waves scattered by surface topography in global seismology (Hudson, 1977) and for surface wave imaging (Snieder, 1987). Its sensitivity in relation to imaging and predicting scattered surface waves in the near-surface is investigated in Blonk and Herman (1994). To account for some variations in the actual depth of the scatterers, we allow the impedance function to depend on frequency. In this way, depth dependence is converted into frequency dependence, much like in a dispersion relation in which vertical structure is related to frequency-dependent velocities. In deriving our Green's function, we reduce the full elastic problem to a scalar problem; therefore, equation 2 is a scalar representation (Appendix A). Thus, we neglect interaction between the vertical and horizontal components of the wavefield.

Los et al. (2001) show that the vertical component of the elastic wavefield generated by a vertical point force can be approximated well by a scalar representation when observed close to the source. When scattering takes place directly at the surface, equation 2 is, in principle, valid for any incident angle (i.e., any wavenumber) of the exciting wavefield  $v(\mathbf{x}'_l, z_1, \omega)$ . Consequently, we can derive the impedance function from an arbitrary reflection and use this function to model the scattered field for all other events. However, the heterogeneities generally are not at the surface, which restricts the use of our method, as is analyzed later in this paper.

### Inverse scattering formulation

Seismic data contain many reflections from deeper layers. All of these events excite surface waves at the same heterogeneities close to the acquisition surface. But in view of the discussion above, we can use the scattered energy from a single event to estimate the impedance function and then use

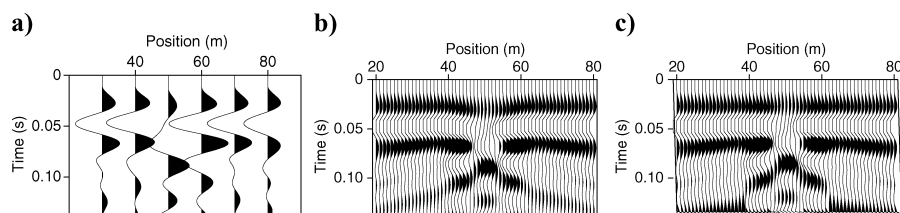


Figure 3. Response of an upcoming plane wave passing through a shallow low-velocity layer with an anomaly (see Figure 2). (a) Vertical velocity at the surface, computed with a 2D elastic finite-difference code and averaged over a distance of 10 m to simulate array forming. (b) Same as (a) but without averaging. The time shift of the first arrival is consistent with the time shift predicted by the statics model. (c) Same as (b) but aligned at first breaks.

this function to predict the scattered energy on every reflection using equation 2. In fact, this is comparable to the approach followed in residual static correction methods, where one selects a (time) window from the data to derive the time shifts for each trace separately. Instead of this single-channel statics operation, we now select one event to derive an impedance function to estimate the scattered energy. (This implies a multichannel operation.)

First, we express the data  $v$  as

$$v(\mathbf{x}, t) = d(\mathbf{x}, t) + r(\mathbf{x}, t), \quad (3)$$

where  $d$  is the selected event and  $r$  denotes the rest of the data. The event  $d$  can be selected by time windowing. We refer to this as the reference event. The reference event should be clearly (visually) discernible. Actually, this is much the same as selecting the data window in residual static correction methods. The window should be long enough to include scattering tails, but ideally it should not include other events. We decompose the reference event  $d(\mathbf{x}, t)$  in a way similar to equation 1:

$$d(\mathbf{x}, t) = d^0(\mathbf{x}, t) + d^1(\mathbf{x}, t), \quad (4)$$

Here,  $d^0$  is the field that would exist without scattering in the near surface and  $d^1$  is the scattered field from heterogeneities in the near surface. How this separation is done hinges on our (assumed) knowledge of the incident wavefield. For instance, if we assume that the upcoming reflections are almost plane events, the separation can be done in the wavenumber-frequency domain. In field data, the reference event can be complicated by propagation effects attributable to traveling from the source to the scattering domain. In such cases, more sophisticated filtering techniques may be required (see Bostock and Rondenay, 1999).

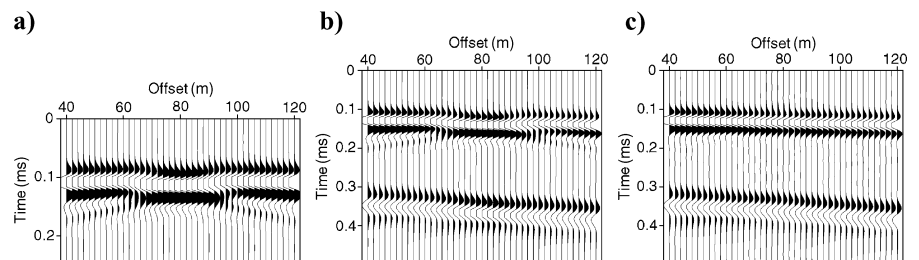
To determine the impedance function, an  $L^2$ -norm is minimized by iteratively updating the impedance function with a conjugate gradient method (e.g., Kleinman and van den Berg, 1991). For the minimization scheme, we write equation 2, for a single event, in the form

$$d^1 = \mathcal{K}\sigma, \quad (5)$$

where  $\sigma$  is the surface impedance function and the operator  $\mathcal{K}$  is defined as

$$\{\mathcal{K}\sigma\}(\mathbf{x}_l, z_0, \omega) = \int_{\mathbf{x}'_l \in \Sigma} u_z^G(\mathbf{x}_l - \mathbf{x}'_l, \Delta z, \omega) \sigma(\mathbf{x}'_l, z_1, \omega) \times d(\mathbf{x}'_l, z_1, \omega) d\mathbf{x}'_l. \quad (6)$$

Figure 4. (a) An upcoming P-wave excites scattered waves; this event is used as our reference event to derive the impedance function. (b) Another event (P- and S-waves) from an angle about  $30^\circ$  from the vertical. This event was not used in deriving the impedance function. (c) Same event as (b) but after subtracting the scattered energy predicted with the impedance function, derived from the scattered energy of the event in (a).



We then minimize the cost function  $F$ , consisting of the squared difference between the observed scattered field and the reconstructed scattered field, and the norm of  $\sigma$ :

$$F = \frac{\|d^1 - \mathcal{K}\sigma\|^2}{\|d^1\|^2} + \lambda\|\sigma\|^2, \quad (7)$$

where  $\lambda$  is a stabilization parameter. By assumption, the scatterers are close to the surface; so in equation 6, we can substitute the field at depth  $z_1$  by the field at the surface  $z_0$ , leaving  $\sigma$  the only unknown. In contrast to Born imaging methods, our method accounts for multiply scattered waves. The impedance function obtained in this way is proportional to the contrast in density between the background medium and the scatterers. Having obtained the impedance function from the strong event, we calculate the scattered field on the whole record using equation 2. Finally, we subtract the scattered field from the data, obtaining the desired output  $v^0$ .

## VALIDATION ON SYNTHETIC DATA

We apply our method to simple models to validate the approximate scattering equation with respect to two major assumptions in deriving the noise model equation 2. We use a 3D elastic modeling scheme (Riyanti and Herman, 2004) to generate the data. Our first assumption is to use a scalar representation, neglecting interaction between vertical and horizontal components of the elastic wavefield. The second assumption is to assume that scattering takes place immediately under the receivers.

First, we consider a shallow scatterer 7.5 m below the surface of a homogeneous elastic half-space. Because the depth of the scatterer is very small, this is mainly a test of the validity of the first assumption. The vertically incident reference (P-wave) event is shown in Figure 4a. From this event, we estimate an impedance function using equation 7. Then, we predict the scattered field on other events with increasing angle of incidence up to about  $30^\circ$  from the vertical.

In Figure 4b, an event with an angle of about  $30^\circ$  is shown. Predicting and subtracting the scattered energy from this event yields the event shown in Figure 4c. The continuity of the target event is restored, implying that we accurately predict the vertical component of the scattered energy, despite the fact that we neglect interaction between vertical and horizontal components in our scalar representation. We also conclude that the method is not sensitive with respect to the angle of incidence when the scatterer is very close to the receiver. Interestingly, the continuity of the S-wave is also restored, using the same impedance function derived from a P-wave.

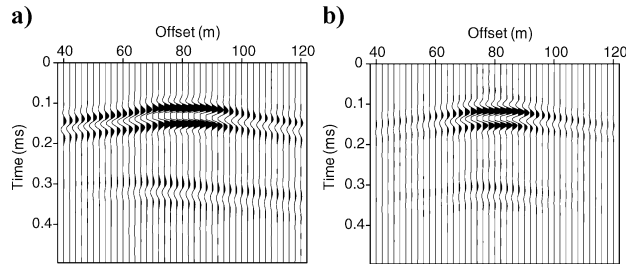


Figure 5. (a) Actual scattered field of the target event with a  $10^\circ$  angle of incidence. (b) Scattered field for the same event, predicted with the estimated impedance function from a vertically incident P-wave reference event (not shown here).

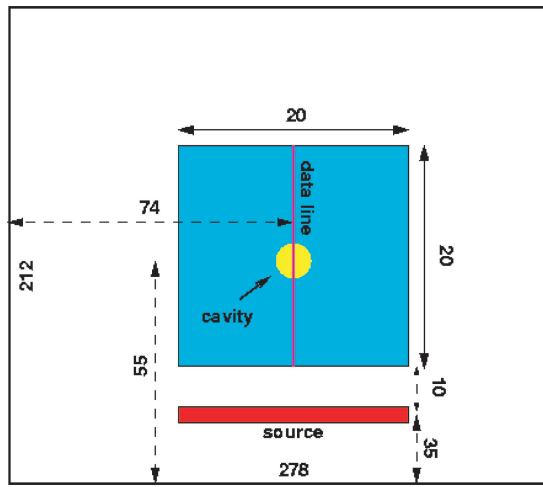


Figure 6. Top view of the aluminum block in experiment 1 with cavity. The shaded area is covered by the receivers. The source width is 0.5 mm. Dimensions are in millimeters.

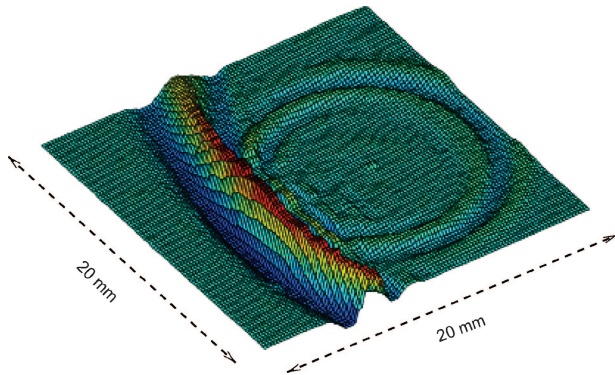


Figure 7. Snapshot of data from the first laboratory measurement in experiment 1 — the vertical component of the direct Rayleigh wave after it passes through the cavity (from right to left). Clearly visible is the circularly expanding scattered Rayleigh wave. The data are recorded at 0.25-mm intervals. The measurement area covers the  $20 \times 20 \text{ mm}^2$  shaded area around the cavity shown in Figure 6.

Next, we consider the same model but with the scatterer about one-half the wavelength of the Rayleigh wave from the surface. Again, we find an impedance function that accurately fits the vertically incident P-wave reference event. However, when we now predict the scattered energy of other events with increasing angles of incidence, the predicted scattered field starts to differ from the actual scattered field for angles larger than  $10^\circ$  from the vertical. In Figure 5a, the actual scattered field for a target event with an angle of incidence of  $10^\circ$  is shown. Figure 5b shows the predicted scattered field for the same event. The main energy in the scattered field is still reasonably well predicted; but since the scatterer is deeper, the approximate equation becomes more sensitive to the relative incident angle between the reference and the target event.

### LABORATORY EXPERIMENTS

#### Description of experiment 1

We measure the vertical velocity on the surface of an aluminum block, excited by a pulsed infrared laser in the thermobatic regime (Scales and Malcolm, 2003). In the first experiment, we consider scattering of surface waves to surface waves only, to ensure maximum control over the scattering process. This is also a test of our method in the case that the exciting wavefield propagates horizontally. We focus the laser beam on a line to simulate a line source. This source generates surface waves that are scattered by a cavity with a diameter of 2 mm and a depth of 3 mm, roughly the size of the dominant wavelength. The wavefield is detected using a scanning laser interferometer that measures the vertical component of the particle velocity on the surface of the model via the Doppler shift (Scales and van Wijk, 1999). Traces are recorded at 0.25-mm intervals, which implies about ten samples per wavelength. Figure 6 illustrates the top view of the experimental configuration; Figure 7 is a snapshot of the wavefield passing through the cavity from right to left, clearly showing the scattered surface wave. [For streaming videos of the experiments described in this paper, refer to Physical Acoustics (2002).]

#### Results from experiment 1

We select an event by time windowing — in this case, the direct Rayleigh wave together with the energy scattered by the cavity (Figure 8a). Depicted in this figure is a portion (41 receivers) of one seismic line (81 receivers) above the cavity. We first estimate the incident wave  $d^0$  using the near-planar character of the incoming wave. For each frequency, a 2D spatial Fourier transformation maps a plane wave to a point in the wavenumber domain. We can use this property to separate the incoming plane wave from its local perturbations, which are attributed to the presence of the cavity. The separated scattered field  $d^1$  is shown in Figure 8b. Clearly, this is an estimate of the true scattered field, limited

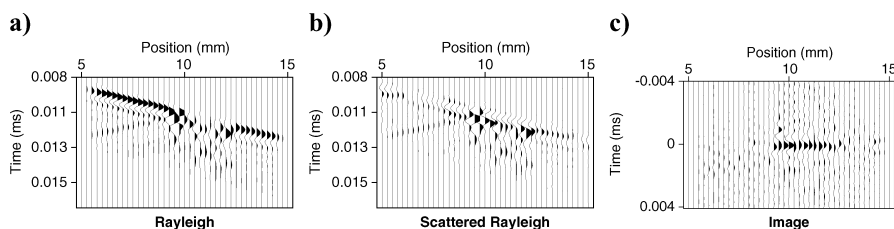


Figure 8. (a) Part of the direct Rayleigh wave (event  $d$  in the text). This event is used to derive the scattered energy  $d^1$ . (b) Separated scattered energy  $d^1$  using a wavenumber frequency-domain filter. (c) Image of the cavity along the same line.

by our separation method, as is evident from the leakage of coherent energy in the separated scattered field of Figure 8b.

Next, we estimate the impedance function using equation 7 and an estimate of the background velocity of the surface waves in aluminum. From the data, we estimate that  $c_R \approx 3000$  m/s. A space–time image of the impedance function for this in-line data set is shown in Figure 8c. From this figure, we learn that the energy is localized in time around  $t = 0$ , which indicates the scatterer is indeed at the surface and the scat-

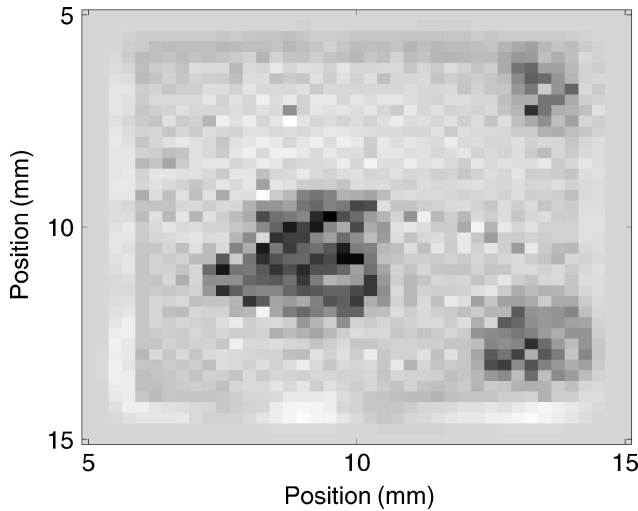


Figure 9. Cross section of the image at  $t = 0$  for the first experiment, showing the correct position and size of the cavity. The two dark-shaded dots in the upper and lower right corners result from scattering from surface disturbances much smaller than the cavity. The darker shades indicate highest amplitudes.

tered energy is focused spatially at the actual location of the cavity. A top view of the image at  $t = 0$  is shown in Figure 9. The circular shape of the impedance function slightly to the left from the center represents the actual shape and location of the cavity (we used a subset of the data not centered exactly around the cavity). Anomalies in the right corners of the figure are the result of scattering from smaller surface disturbances.

Having obtained an estimate of the spatial impedance function from the direct Rayleigh wave, we now calculate the scattered wavefield  $v^1$  for a different event. This event has not been used to determine the impedance function; therefore, prediction of the scattered field for this other event is a good validation of the method. We select the Rayleigh wave that is reflected by the end of the aluminum block behind the source. We call this event the ghost (Figure 10a). The predicted scattered field is shown in Figure 10b. Finally, we obtain the wavefield minus the scattered energy from equation 1, shown in Figure 10c. The scattering has been effectively removed, and the continuity of the event has increased.

### Description of experiment 2

In the second experiment, we consider scattering of upcoming body waves by near-surface heterogeneities. Body waves are excited by a point source at the bottom of a two-layered model, consisting of an aluminum layer, topped by a Lucite layer, in which we drill a 2-mm-wide and 3-mm-deep cavity. When the body waves reach the surface, energy is scattered by the cavity. We record the wavefield in a 4-cm<sup>2</sup> region at 0.1-mm intervals.

Compared to experiment 1, these data are further complicated because they contain multiples from the layer boundary and reflections from the sides of the model, as depicted in Figure 11b. Data above the cavity (Figure 12) show the multiples

Figure 10. (a) The ghost Rayleigh wave. (b) The predicted scattered field for this event. (c) The ghost Rayleigh wave after removing predicted near-surface scattering.

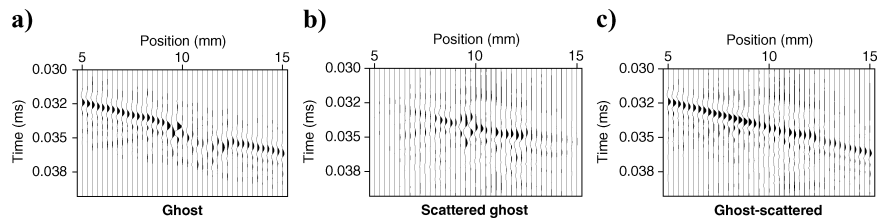
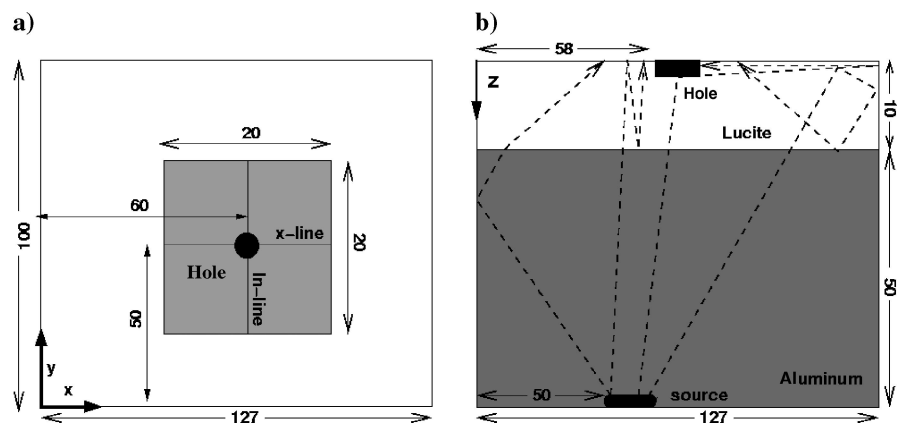


Figure 11. (a) Top and (b) side view of the two-layered model with a cavity. Dimensions are in millimeters.



between the layers and reflections from the sides being scattered by the cavity. Because the source is at the bottom of the model and the body waves are only partly transmitted through the aluminum-Lucite interface, the received signal is much weaker than in the first experiment. For this reason, these data require some preprocessing, consisting of tapering off low frequencies (including a dc component) and then applying a short spatial convolution filter to increase S/N ratio. Here, the spatial sampling is dense and the convolution filter is only three traces in each of two perpendicular directions, so it is not comparable to the array-forming discussed earlier and does not significantly affect the results of our method.

**Results from experiment 2**

The data from experiment 2 present a more challenging test for our method, containing features observed in field seismic data, such as multiples, low S/N ratio, and interfering events from various angles. Apart from preprocessing the data, the algorithm is applied in the same way as for experiment 1.

Again, we start by selecting a clear event. In this case, we select the first upcoming event (Figure 13a). We separate the incoming  $d^0$  from the energy scattered by the cavity  $d^1$  using a narrow wavenumber–frequency-domain filter. The separated scattered field is shown in Figure 13b. Using the surface-wave velocity of Lucite ( $c_R \approx 1000$  m/s), we estimate the impedance function (Figure 13c). Here, we window the impedance function in the time domain to reduce ringing in the predicted scat-

tered field (some frequencies may be dominant in the image). Figure 14 is a top view of the image at the surface at  $t = 0$ . The dimensions and location of the image agree with the actual location and shape of the cavity.

Finally, we predict the near-surface scattered field in the rest of the data. Depicted in Figure 15a are part of the data on a line above the cavity. The data shown in this figure were not used to derive the impedance function. Our method is sensitive to the velocity of the surface wave because, as we subtract the modeled scattered waves, a small error in the surface-wave velocity may cause constructive interference with the surface waves in the actual data. The same holds true for velocity variations from dispersion. For this reason, the desired result may contain residual tails from surface waves, but these can be removed by dip filtering. However, to remove the apexes of the scattering only, we find that an accurate velocity is less important.

So to make a comparison between the data before and after applying the algorithm, we use a dip filter on the input data  $v$  as well as on the data after removal of scattered surface waves. The filtered input data are shown in Figure 15b. Obviously, the dip filter only removes the flanks of the surface waves but not the apexes, which have higher apparent velocities and are therefore unaffected by the filter. This part of the surface waves is especially important to remove because the interference between surface-wave scattering and the incident field diminishes the quality of the target reflector. The output  $v^0$  after applying our method, followed by the same dip filter, is shown in Figure 15c. We conclude that the algorithm improves the continuity of the reflectors.

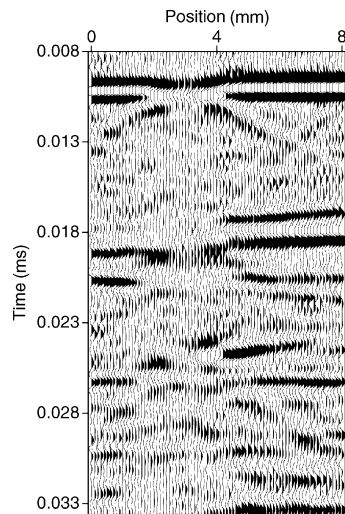


Figure 12. Seismogram of part of the data through the cavity.

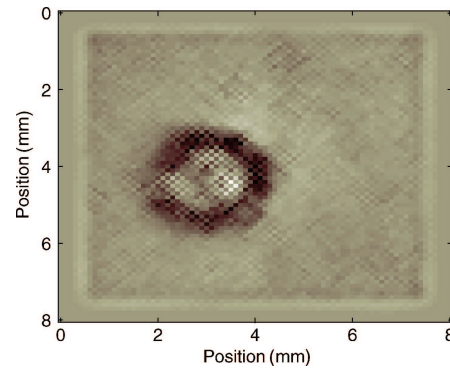


Figure 14. Top view of the image at  $t = 0$  for experiment 2, showing the correct position and dimensions of the actual cavity.

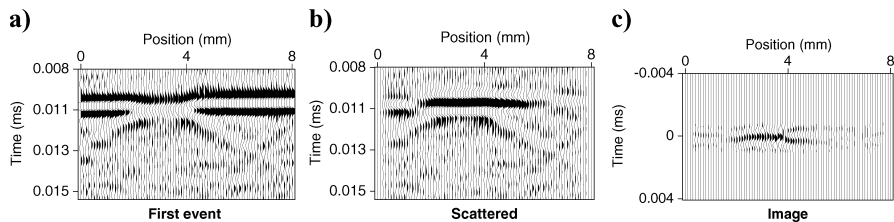


Figure 13. (a) The first upcoming event from the data (event  $d$  in the text). This event is used to derive the scattered energy. (b) Separated scattered energy  $d^1$  using a narrow wavenumber frequency-domain filter. (c) Image of the cavity along the same receiver line

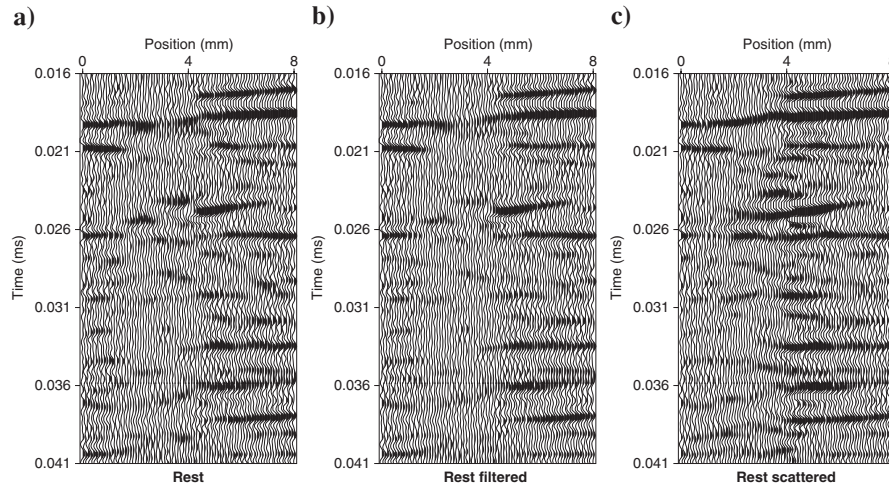


Figure 15. (a) Part of the rest of the record. (b) Same as in (a) but after dip filtering to attenuate surface waves. (c) Same as (a) but after subtracting near-surface scattered energy, followed by the same dip filter as in (b).

## CONCLUSIONS

We have described a method to suppress scattered surface waves excited by body-wave reflections. We formulated a scalar representation for the scattered noise involving the vertical component of the particle velocity only. If the scattering takes place directly under the receivers, we can approximate the field at the scattering depth by the recorded field at the surface. Using 3D elastic synthetic data, we showed that the results of our method are consistent with the assumptions. For shallow scatterers, we completely restored the continuity of a P- and S-wave reflection using an impedance function derived from an independent P event. Using data from a laboratory-scale, surface-wave scattering experiment, we estimated the impedance function of a cavity in the surface of an aluminum block using the direct Rayleigh wave, measured with densely deployed receivers. This impedance function was then used to restore the continuity of a reflected Rayleigh wave that was not used to estimate the impedance function. A second experiment with a layered model was conducted to generate a data set with upcoming body waves from various directions that were scattered by a cavity in the top layer. These data contained features also observed in seismic field data. Application of the algorithm improved the continuity of the upcoming events in these more complicated data.

We now plan to direct our efforts to applying the algorithm to high-resolution field data. From our experience with the ultrasonic data, we expect the main difficulty in applying our method to field data will be to extract near-surface scattered energy from an event, especially in the presence of surface topography.

## ACKNOWLEDGMENTS

We thank Shell International E & P (SIEP) and Wim Mulder of SIEP for the use of the finite-difference code used in

the first synthetic example and Dwi Riyanti (Delft University) for her help in computing the data in the second synthetic example. Part of the work presented in this paper was carried out while X. Campman was a visitor in the Physical Acoustics Laboratory (PAL) at Colorado School of Mines. He thanks everyone at PAL and the Center for Wave Phenomena for their hospitality and many fruitful discussions. The work of X. Campman was supported by the Dutch Technology Foundation (STW). The work at PAL was supported by the National Science Foundation (EAR-0111804) and the U.S. Army Research Office (DAAG55-98-1-0070). K. van Wijk acknowledges U. S. Army Research Office support under contract DAAD19-03-1-0292.

## APPENDIX A

### GREEN'S FUNCTION

We start with the wave equation for the vertical component of particle displacement  $u_z$  from a vertical point force  $f_z$  in an isotropic, (laterally) homogeneous, elastic solid in the frequency domain:

$$(\lambda + \mu)\partial_z(\partial_x u_x + \partial_y u_y + \partial_z u_z) + \mu\nabla \cdot \nabla u_z(\mathbf{x}, \omega) + \rho(\mathbf{x})\omega^2 u_z(\mathbf{x}, \omega) = -f_z(\mathbf{x}, \omega). \quad (\text{A-1})$$

The operator  $\nabla = (\partial_x, \partial_y, \partial_z)$  contains the spatial derivatives, and  $\omega$  denotes angular frequency. Here, the kernel in the Fourier transformation is  $\exp(-i\omega t)$ . The Lamé parameters,  $\lambda$  and  $\mu$ , are assumed constant. The associated compressional-wave velocity is  $c_P = \sqrt{(\lambda + 2\mu)/\rho}$  and the shear-wave velocity  $c_S = \sqrt{\mu/\rho}$ . For upcoming reflections we assume the vertical component dominates the horizontal components and, consequently, interaction between the vertical and horizontal components at the scatterer can be neglected.

By introducing the scaled vertical coordinate  $\zeta = (c_S/c_P)z$ , equation A-1 can be reduced to the scalar Helmholtz equation:

$$(\nabla^2 + k^2)u_z(\mathbf{x}_l, \zeta, \omega) = -\frac{1}{\mu}f_z(\mathbf{x}_l, \zeta), \quad (\text{A-2})$$

where  $\mathbf{x}_l = (x, y)$  is the horizontal position vector and we have introduced the wavenumber  $k^2 = \omega^2/c_S^2$ . In the operator  $\nabla$ , the derivative with respect to the vertical coordinate  $\partial_z$  is replaced by  $\partial_\zeta$ . The Green's function is defined as the solution to

$$(\nabla^2 + k^2)u_z^G(\mathbf{x}_l, \zeta, \omega) = -\delta(\mathbf{x}_l - \mathbf{x}'_l)\delta(\zeta - \zeta'). \quad (\text{A-3})$$

After a Fourier transformation with kernel  $\exp(i\mathbf{k}_l \cdot \mathbf{x}_l)$ , equation A-3 reads

$$(\partial_\zeta \partial_\zeta + k_z^2)u_z(\mathbf{k}_l, \zeta, \omega, \mathbf{x}'_l, \zeta') = -\delta(\zeta - \zeta') \exp(-i\mathbf{k}_l \cdot \mathbf{x}'_l), \quad (\text{A-4})$$

where  $k_z^2 = k^2 - k_x^2 - k_y^2$  and the horizontal wavenumbers are denoted by  $\mathbf{k}_l = (k_x, k_y)$  and where  $i$  is the complex unit  $\sqrt{-1}$ . Equation A-4 is subject to the boundary conditions of a traction-free half-space, leading to the condition

$$\partial_\zeta u_z = 0, \quad \zeta = 0. \quad (\text{A-5})$$

The solution is given by

$$u^G(k_x, k_y, \zeta, \omega, \mathbf{x}') = \frac{1}{2ik_z} [\exp(-ik_z|\zeta - \zeta'|) + \exp(-ik_z|\zeta + \zeta'|)] \exp(-i\mathbf{k}_l \cdot \mathbf{x}'_l), \quad (\text{A-6})$$

with  $\text{Re } k_z > 0$  and  $\text{Im } k_z < 0$ , on account of the radiation condition at infinity (Bleistein et al., 2001) and our Fourier transformation conventions.

The integral in equation 2 can be calculated efficiently using the convolution theorem. Therefore, we calculate the Green's function in the horizontal wavenumber-frequency domain as given in equation A-6. In order not to complicate the main text, we use  $z$  to denote the scaled depth, instead of  $\zeta$ , from equation 2 onward.

## REFERENCES

Aki, K., and P. G. Richards, 1980, Quantitative seismology: Theory and practice: W. H. Freeman & Co.  
 Baeten, G., V. Belougne, L. Combee, E. Kragh, A. Laake, J. Martin, J. Orban, A. Ozbek, and P. L. Vermeer, 2000, Acquisition and processing of point receiver measurements in land seismic: 62nd Annual Meeting, European Association of Geoscientists and Engineers, Extended Abstracts, B-06.  
 Baeten, G. J. M., L. Combee, and L. West, 2001, Static perturbation corrections on single sensor data: 63rd Annual Meeting, European Association of Geoscientists and Engineers, Extended Abstracts, IS-01.  
 Blacquière, G., and L. Ongkiehong, 2000, Benefits of single sensor recording: 62nd Annual Meeting, European Association of Geoscientists and Engineers, Extended Abstracts, B-07.  
 Bleistein, N., J. K. Cohen, and J. W. Stockwell Jr., 2001, Mathematics of multidimensional seismic imaging, migration and inversion:

Springer-Verlag.  
 Blonk, B., and G. C. Herman, 1994, Inverse scattering of surface waves: A new look at surface consistency: *Geophysics*, **59**, 963–972.  
 Bostock, M. G., and S. Rondenay, 1999, Migration of scattered teleseismic body waves: *Geophysics Journal International*, **137**, 732–746.  
 Combee, L., 1994, Wavefield scattering by a 2-D near-surface elliptic anomaly: 64th Annual International Meeting, SEG, Expanded Abstracts, 1306–1309.  
 ———, 1995, Scattering of the source-generated wavefield by a 2-D near-surface elliptic anomaly: 65th Annual International Meeting, SEG, Expanded Abstracts, 1325–1328.  
 Cox, M. J. G., 1999, Static corrections for seismic reflection surveys: SEG.  
 Gupta, I. N., C. S. Lynnes, T. W. McElfresh, and R. A. Wagner, 1990,  $f$ - $k$  analysis of NORESS array and single station data to identify sources of near-receiver and near-source scattering: *Bulletin of the Seismic Society of America*, **80**, 2227–2241.  
 Herman, G. C., P. A. Milligan, Q. Dong, and J. W. Rector, 1999, Analysis and removal of multiply scattered tube waves: *Geophysics*, **65**, 745–754.  
 Hudson, J. A., 1977, Scattered waves in the coda of P: *Journal of Geophysics*, **43**, 359–374.  
 Kennett, B. L. N., 2002, The seismic wavefield—Volume II: Interpretation of seismograms on regional and global scales: Cambridge University Press.  
 Kleinman, R. E., and P. M. van den Berg, 1991, Iterative methods for solving integral equations: *Radio Science*, **26**, 175–181.  
 Levander, A. R., 1990, Seismic scattering near the earth's surface: *Pure and Applied Geophysics*, **132**, 21–47.  
 Los, H. S., G. C. Herman, and P. Hölscher, 2001, Dynamic interaction between train wheels and the subsurface: *Journal of Sound and Vibration*, **247**, no. 5, 917–926.  
 Physical Acoustics Laboratory, Colorado School of Mines, 2004: (28 October 2004, <[http://acoustics.mines.edu/publine\\_one\\_scatterer\\_long.mpg](http://acoustics.mines.edu/publine_one_scatterer_long.mpg)>).  
 Regone, C. J., 1998, Suppression of coherent noise in 3-D seismology: *The Leading Edge*, **17**, 1584–1589.  
 Riyanti, C. D., and G. C. Herman, 2004, 3-D elastic modeling of near-surface scattering: 66th Annual Meeting, European Association of Geoscientists and Engineers, Extended Abstracts, P093.  
 Scales, J. A., and A. Malcolm, 2003, Laser characterization of ultrasonic wave propagation in random media: *Physics Review E*, **67**, 046618.  
 Scales, J. A., and K. van Wijk, 1999, Multiple scattering attenuation and anisotropy of ultrasonic surface waves: *Applied Physics Letters*, **74**, 3899–3901.  
 Snieder, R. K., 1987, Surface wave holography, in G. Nolet, ed., *Seismic tomography, with applications in global seismology and exploration geophysics*: D. Reidel Publishing Co., 323–337.  
 Wagner, G. S., and C. H. Langston, 1992, Body-to-surface-wave scattered energy in teleseismic coda observed at the NORESS seismic array: *Bulletin of the Seismic Society of America*, **82**, 2126–2138.  
 Yilmaz, O., 1987, *Seismic data processing*: SEG.

NO PRINTING